Trapping ions from a fast beam in a radio-frequency ion trap: The relaxation of the ion cloud and its resulting column density

Annette Svendsen, Kristian M. E. Nielsen, and Henrik B. Pedersen*
Department of Physics and Astronomy, Aarhus University, DK-8000 Aarhus C, Denmark
(Received 3 April 2014; published 12 June 2014)

The relaxation of trapped Cl_2^- ions and their resulting column density in a multipole radio-frequency (RF) ion trap have been investigated after loading the trap from an initial fast-moving beam exploiting a mechanism described recently [A. Svendsen *et al.*, Phys. Rev. A **87**, 043410 (2013)] where the injection is mediated through the exchange of energy between ions and the oscillating RF field. The temporal relaxation of the energy distribution of the trapped ion cloud was probed by observing the evolution of the resulting time-of-flight distribution of ions after extraction and fragment mass analysis in a quadrupole mass filter. The ion energy distribution was found to be essentially stationary after ∼20 ms. The resulting column density of trapped ions after relaxation was probed by two-dimensional position-resolved photodissociation of the trapped Cl_2^- ions. A detailed statistical analysis of the ion column density in the ring-electrode trap is given, and by comparison to the experimental data, a value of the maximum adiabaticity parameter of $\eta_{\max} \simeq 0.28$ is inferred. It is further demonstrated how the present experimental system allows for time-resolved mass spectrometry by probing explicitly the populations of both parent (Cl_2^-) and daughter (Cl^-) ions as a function of time after closing the trap and after laser irradiation. Finally, it is discussed how the setup can be used to obtain absolute photodissociation cross sections via a tomographic method without assumptions on the decay law for the trapped ions.

DOI: 10.1103/PhysRevA.89.063410 PACS number(s): 37.10.Ty, 32.80.Gc

I. INTRODUCTION

Since the first demonstration [1] of confinement of charged particles between electrodes with potentials oscillating at radio frequencies (RF), the application of RF-based trapping, guiding, and mass selecting devices have proven extremely important in wide areas of physics and chemistry (see, for instance, Refs. [2,3]). In particular within molecular physics where cooling of both external and internal degrees of freedom of molecular ions is needed, multipole traps [2] are heavily used. With these traps, the part of the ion motion oscillating with the frequency of the RF field, the so-called micromotion, can be suppressed which in turn allows for efficient cooling by collisions of the trapped ions with a thermalized buffer gas (typically He) [4]. The deceleration of ions by collisions with a buffer gas is furthermore often used to facilitate the initial injection of ions into the RF trap.

The use of buffer gas becomes problematic, however, when ions are to be extracted from the RF trap, since cooled ions may heat up in collisions during the extraction process. Additionally, if the trapped ions are subject to ionizing radiation (e.g., high-energy photons), a significant (dominant) ionization of the dense buffer gas also occurs which may lead to unwanted effects.

In a previous paper [5], we described the injection of ions into a ring-electrode (multipole) RF trap [2] without the use of a buffer gas for deceleration by exploring explicitly the energy exchange between the incoming ions and the longitudinal component of the oscillating RF field in analogy to charged-particle motion in a linear accelerator [6]. Consequently, the resulting ensemble of trapped ions emerges with an energy distribution that is evidently *nonthermal*, i.e., can not be described by a Boltzmann distribution, but rather reflects the overall effect of the detailed acceleration or deceleration. In general, the energy distributions expected from the newly described mechanism [5] of injection are wider and flatter as compared to a Boltzmann distribution at or below room temperature. In the limit of low ion density in the trap, Coulomb repulsion between the ions can be neglected, and the behavior of an ensemble of trapped ions is then entirely determined by the energy distribution. In this situation, the stored ions only interact with the trapping electric field which is in contrast to trapped ions cooled by a buffer gas which influences the properties of the ion cloud.

In this paper, we investigate in more detail the properties of a trapped ensemble of Cl_2^- ions after injection with the mechanism described in Ref. [5]. Thus, we observe the relaxation of the trapped ions as a function of time after injection, and probe the column density of ions after relaxation by photodissociation ($Cl_2^- + 532$ nm $\rightarrow Cl^- + Cl^0$) throughout the transverse plane of the trap.

The present realization of the ring-electrode trap, the description of trapped ion motion [2], as well as the injection mechanism were reviewed and presented in detail in Ref. [5]. Central to a simple description of ion motion in a RF trap is the adiabatic approximation, where the fast oscillating *micro*motion of an ion in the RF field is separated from the *drift* motion which can be described through an effective potential U_{eff}. For the cylindrically symmetric ring-electrode trap, the ion position inside the trap volume is described by reduced coordinates in the longitudinal $\hat{z} = z/z_0$ and transverse $\hat{r} = r/z_0$ directions, where $2\pi z_0 = 4$ mm is the distance between neighboring ring electrodes of the same RF phase [see Fig. 1(a)]. The effective potential can be written explicitly as

$$U_{\text{eff}}(\hat{r},\hat{z}) = \frac{(qe)^2 V_0^2}{4m\omega^2} u_{\text{eff}}(\hat{r},\hat{z}), \quad (1)$$

*To whom correspondence should be addressed: hbjp@phys.au.dk

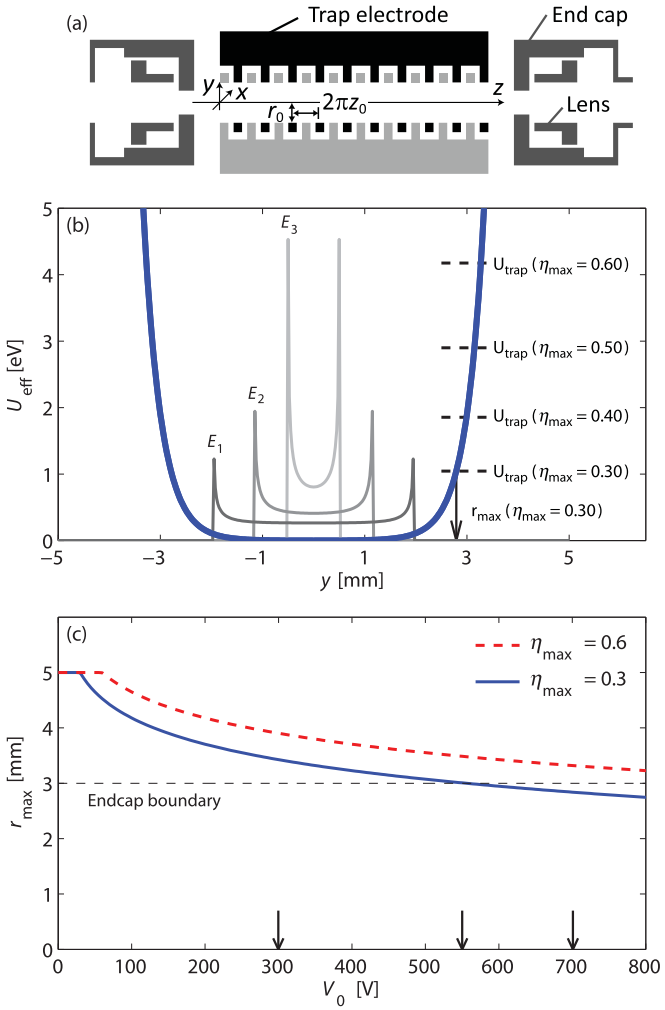

FIG. 1. (Color online) Trapping of ions in the ring-electrode trap. (a) Schematic of the ring-electrode trap showing the geometrical quantities characteristic for the ring-electrode trap, $r_0 = 5$ mm and $2\pi z_0 = 4$ mm. (b) The effective potential across the transverse plane of the RF trap (thick blue line) at a high RF amplitude of $V_0 = 750$ V. The trap depth $U_{\rm trap}$ [5] for various assumptions on the maximum adiabaticity parameter $\eta_{\rm max}$ is indicated with the dashed lines, and the maximum radius $r_{\rm max}$ of the ion cloud for $\eta_{\rm max} = 0.3$ is indicated with the arrow to the horizontal axis. The gray scaled solid lines show single-ion densities for total mechanical energies of $E_1 = 10^{-3}$ eV, $E_2 = 10^{-2}$ eV, and $E_3 = 10^{-1}$ eV. (c) Radius of the the adiabatic region in the RF trap as a function of the RF amplitude [5] for two different assumptions on the maximum value of the adiabaticity paramter $\eta_{\rm max}$. The arrows pointing to the horizontal scale indicate values of the RF amplitude explored in this work.

where m and qe are the ion mass and charge, $\omega = 4\pi \times 4$ MHz, and V_0 are the angular frequency and amplitude of the RF potential, and the detailed form of the function $u_{\rm eff}(\hat{r},\hat{z})$ can be found in [5] [its Eq. (7)]. The range of validity of the adiabatic approximation is quantified through the limit on the so-called adiabaticity parameter, i.e., $\eta < \eta_{\rm max}$. For the ring-electrode trap, the adiabaticity parameter is

$$\eta(\hat{r},\hat{z}) = \frac{2|qe|V_0}{m\omega^2}\hat{\eta}(\hat{r},\hat{z}), \qquad (2)$$

where also the detailed form of the function $\hat{\eta}(\hat{r},\hat{z})$ can be found in Ref. [5] [its Eq. (8)].

Figure 1(b) displays the effective potential (solid blue line) for a high value of the RF amplitude, at $x = 0$ and $\hat{z} = 2\pi$. For a particular limiting value of η, ions can be trapped up to a certain radius $r_{\rm max}$ below which the ion motion can be considered adiabatic. This consequently gives rise to an effective trap depth $U_{\rm trap}$ of the effective potential for a given value of $\eta_{\rm max}$, as indicated on the right side of Fig. 1(b). This maximum radius is shown in Fig. 1(c) for two choices of $\eta_{\rm max}$. At low values of the RF amplitude, the maximum radius coincides with the inner radius $r_0 = 5$ mm of the ring electrodes. The gray scaled curves in Fig. 1(b) illustrate the one-dimensional spatial distribution of single ions at different energies in RF trap. From the measurements of column densities in this study, we obtain information on the maximum value of the adiabaticity parameter for the present RF trap.

The present experimental results demonstrate that the dynamics of the trapped ions is indeed strongly influenced by the initial energy distribution imposed by the injection mechanism. Thus, the loss of ions from the trap is described by a power-law time dependence characteristic of an inhomogeneous decay mechanism as expected for nonthermalized ions. The trapped ensemble of ions relaxes strongly for ca. 18–20 ms, after which the resulting column densities are consistent with distributions expected for a maximum adiabaticity parameter of ~0.28.

II. EXPERIMENT

Cl_2^- ions were produced in a Aarhus Negative Ion Source (ANIS) [7] (a sputter ion source) using a hollow Cu-cathode filled with a pressed powder of a 1:1 mixture of AgCl and Cu. The source was operated with a 1-mm-diameter tungsten filament heated by a dc current of 38–40 A leading to an overall temperature of the water-cooled source of ~400 K. The ANIS was operated with a transverse magnetic field of ~80 mT, and with a sputter cathode potential of $V_S = -2$ kV. The ion source was located on a high-voltage platform kept at a potential of $V_{\rm HV} = -1$ kV, and by extraction to ground potential, a fast beam of negative ions of kinetic energy $K_0 = qe\,(V_{\rm HV} + V_S) = 3$ keV was formed, where $q = -1$. This monoenergetic ion beam was deflected 90° by passage through a magnetic field which separates ions according to their mass-to-charge ratio. The result of the mass selection was a beam of Cl_2^- of ~0.3 nA which was further steered and focused towards the entrance of the RF trap. For comparison, a current of ~130 nA was obtained of atomic Cl^- from the ion source.

The experimental system around the RF trap, where ions and laser pulses are brought to interact, is shown schematically in Fig. 2. During the reported measurements, the residual gas pressure in the ion trap chamber was kept at $\sim 1.0\times10^{-8}$ mbar corresponding to a residual gas density of $\sim 2.4\times10^{8}$ cm^{-3}.

The RF-trap assembly has been described in detail previously [5], and consists of a ring-electrode trap [2] with a specially adapted end-cap electrode geometry which includes electrodes for focusing of the incoming fast ion beam and for facilitating ion extraction from the trap. Compared to the setup described in Ref. [5], the present experimental setup has been expanded with the addition of a quadrupole mass spectrometer (QMS) and further adaptive ion optics on the exit side of the

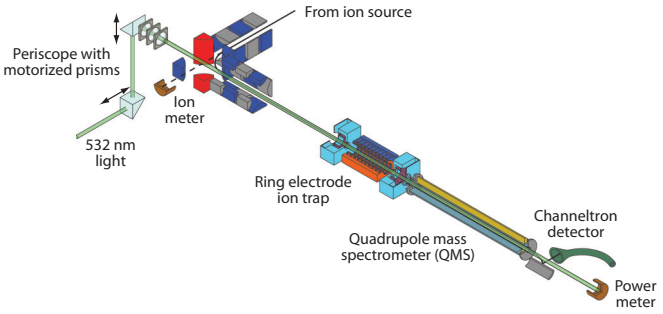

FIG. 2. (Color online) Illustration of the central part of the experimental setup with the RF trap and the adjacent quadrupole mass spectrometer (QMS) and channeltron detector. Ions are injected into the RF trap by the method described in Ref. [5]. The ion current can be measured continuously between injections, and the laser intensity is measured behind the channeltron.

ion trap. Single ions ejected from the trap pass through the mass spectrometer and are electrically bent into a channeltron detector. Their time-of-flight (TOF) relative to the extraction trigger is registered with the data acquisition system. The entire setup comprising the trap, QMS, and channeltron detector is kept at a high potential V_{trap} relative to ground as the fast ions must be decelerated in order to be confined in the somewhat shallow trapping potential (trap depth is of the order of a few eV). In the absence of energy exchange between ions and the trapping RF field, the kinetic energy of an ion arriving at the trap center would be $K_{\text{stat}} = K_0 - qV_{\text{trap}}$.

The combined system of the RF trap and the QMS allows for ion trapping followed by mass analysis of the stored ensemble of ions after a variable trapping time by extracting the stored ions through the QMS. An example of the mass spectrum obtained after a trapping time of 20 ms is shown in Fig. 3. These data illustrate explicitly the presence of both parent ions (Cl_2^-) and daughter ions (Cl^-) resulting from dissociation of parent ions.

For the photodissociation experiments reported here, the stored Cl_2^- ions were irradiated along the trap axis (the z axis) by a laser pulse at a time $t_L = 18.2$ ms after closing the trap.

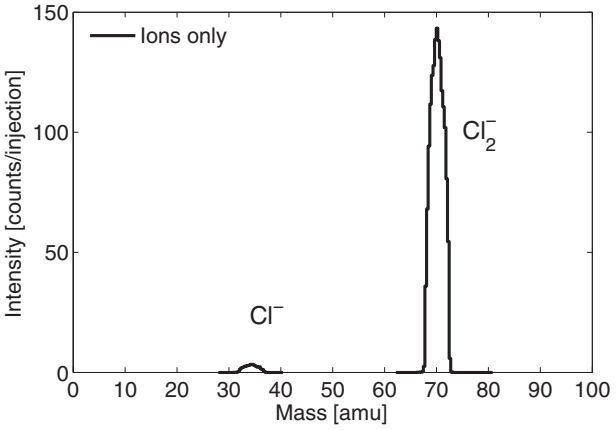

FIG. 3. Mass spectrum of trapped ions obtained with the quadrupole mass spectrometer after a trapping time of 20 ms, showing the presence of primarily parent ions (Cl_2^-) and also *spontaneously* formed daughter ions (Cl^-) (see also Fig. 6).

The laser pulses were derived as the second harmonic of a commercial Nd:YAG laser system and had a width of $w_L \sim 3$ ns, were horizontally polarized, and had a photon energy of $E_\lambda = 2.33$ eV (532 nm). Typical total laser pulse energies were $E_p = 4$–8 mJ/pulse. In this regime, the laser-induced ion signal was measured to be proportional to the laser pulse energy which is consistent with single-photon absorption.

The laser light was guided and slightly focused into the ion trap using several prisms and lenses. In particular, as illustrated in Fig. 2, the last optical stage before entering the vacuum system was a periscope where both the horizontal (x_L) and vertical (y_L) output positions of the light were adjustable in a region of ± 12.5 mm from the trap center axis. Moreover, a telescope for adjusting the focus of the laser light inside the RF trap was fixed directly to the last prism of the periscope. In this way, the direction and focusing of the light were kept separate and the transverse intensity profile of the light pulses reaching the interaction region was independent of the setting of the periscope. With the adapted distances, where the last optical element was located ~ 1 m from the trap center, the focusing was such that the transverse profiles of the light pulses were essentially constant over the longitudinal extent (<50 mm) of the ion cloud in the RF trap. Behind the channeltron detector, the laser beam was dumped into a power meter which recorded the average laser intensity.

The actual horizontal and vertical profiles of the laser pulses in the trap region were determined by scanning the laser pulses across the edge of the end-cap electrode (see Fig. 2) on the entrance side of the RF trap while observing the laser intensity $I(x_L, y_L)$ behind the trap. Assuming the horizontal and vertical laser intensity profiles to be independent, the spatial laser intensity distribution can be factorized as $g(x,y) = g_x(x)g_y(y)$, and the total (unblocked) laser intensity can be expressed as

$$I_0 = \int_{-\infty}^{\infty}\int_{-\infty}^{\infty} g_x(x)g_y(y)dx\,dy. \tag{3}$$

The laser position is now scanned vertically across the center ($x_L = 0$) of the end-cap electrode, the boundary of which is located at $y = \pm y_{\text{cap}} (= \pm 3$ mm). Since the inner diameter of the end-cap electrode (6 mm) is much larger than the actual extent of the laser profile (diameter ~ 0.7 mm), the measured laser intensity I at position $u_L = y_L + y_{\text{cap}}$ [see Fig. 4(a)] is then given by

$$\begin{aligned} I(u_L) &= \int_{-\infty}^{\infty} g_x(x - x_L)dx \int_{-y_{\text{cap}}}^{y_{\text{cap}}} g_y(y - y_L)dy \\ &= \int_0^{2y_{\text{cap}}} g_y(u - u_L)du. \end{aligned} \tag{4}$$

The corresponding measured laser intensity is displayed in Fig. 4(b). The transverse intensity profile $g_y(y)$ can now be obtained directly from this measurement as the derivative, i.e.,

$$\begin{aligned} \frac{d}{du_L} I(u_L) &= -\int_0^{2y_{\text{cap}}} \frac{dg_y(u - u_L)}{du} du \\ &= g_y(u_L) - g_y(u_L - 2y_{\text{cap}}) \\ &= g_y(u_L) \quad \text{for} \quad |u_L - 2y_{\text{cap}}| \gg \sigma_y, \end{aligned} \tag{5}$$

where the last expression is valid when the laser is positioned close to the lower edge of end-cap electrode (u_L close to zero).

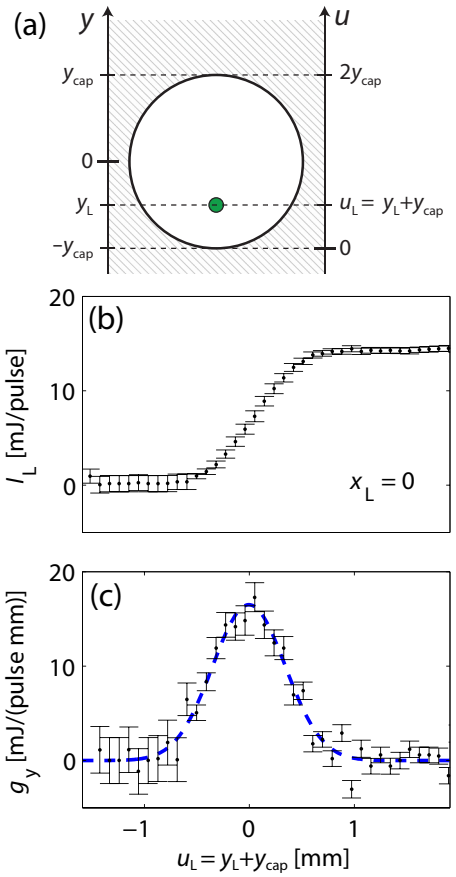

FIG. 4. (Color online) Measurement of the vertical laser profile by scanning the laser across the edge of the end-cap electrode. (a) Schematic illustration of the position of the laser [green (gray) dot] inside the opening of the end-cap electrode. (b) Laser intensity measured behind the RF trap and QMS (see also Fig. 2) obtained with the laser horizontally fixed at $x_L = 0$ mm while scanning the laser vertical position y_L. (c) Differentiated intensity being proportional to the vertical laser profile [Eq. (6)]. The dashed line shows a Gaussian fit to the intensity profile. Similar measurements were done to obtain the horizontal profile.

The resulting experimentally determined vertical laser pulse profile is shown in Fig. 4(c), which also shows a Gaussian fit with spread of $\sigma_y = 0.35 \pm 0.01$ mm. Similarly, the horizontal laser profile was found to be well represented by a Gaussian distribution with spread of $\sigma_x = 0.32 \pm 0.01$ mm.

To measure the relative column density of ions in the RF trap, the transverse position (x_L, y_L) of the laser pulses was systematically scanned across the accessible region of the RF-trap volume while simultaneously recording the photofragmentation yield of Cl^- ions by extraction and mass analysis in the QMS.

The experimental system was operated at a total rate of 20 Hz with four alternating cases (5 Hz each) of (1) both ions and laser pulse present in the trap (giving N^u_{IL} counts after extraction), (2) ions only (N^u_I), (3) laser only (N^u_L), and (4) neither ions nor laser, i.e., dark counts (N^u_D). For a given measurement, the QMS setting determines what ion species is detected, either Cl^- or $Cl_2{}^-$, and the detected ion species is indicated by the superscript u. By combining these measurements, the background-corrected laser-induced ion yield of species u, N^u_S, is expressed as

$$N^u_S = N^u_{IL} - N^u_I - N^u_L + N^u_D. \tag{6}$$

This quantity was then measured as a function of the laser position. The dominating background originates from the *ions-only* case (N^u_I), while only minor background counts on the channeltron were observed under the cases of *laser only* and *dark counts*.

In order to suppress possible short-term fluctuations in laser pulse energy and the number of trapped ions, each point in a measurement series was typically averaged over 100 trap loadings (implying that each of the four cycles described above were repeated 100 times). Long-term variations were averaged out by repeating each measurement series several times. For example, the two-dimensional profiles presented in Fig. 7 have been measured several times, and each point represents an average of approximately 500 trap loadings.

III. RESULTS

A. Spontaneous evolution of trapped ions

The evolution of the number of trapped *parent* ions ($Cl_2{}^-$) as a function of time after closing the trap is displayed in Fig. 5(a). The observed decay with only ions present in the RF trap [red dots in Fig. 5(a)] shows a strong decrease within the first 1 ms after which the decay curve can be very well represented by a power law of the form

$$N^{Cl_2{}^-}_I(t) = A_0(t/t_0)^{-1/n}. \tag{7}$$

Here, $t_0 = 1$ ms to make A_0 dimensionless, and the best fit to the experimental decay curve yields $n = 11.7 \pm 0.2$ and $A_0 = 106.5 \pm 0.4$. This type of decay law is characteristic of an inhomogeneous ensemble of trapped particles where in this case the trapped ions have different probabilities for escaping the trap depending on their individual properties.

The injection mechanism applied in this experiment [5] indeed gives rise to a wide energy distribution of the trapped ions, which naturally results in an inhomogeneous loss mechanism, for instance, represented by an energy-dependent escape rate k_E. Formulated explicitly, the evolution of the total number of trapped parent ions $N^{Cl_2{}^-}_I$ in the absence of a laser pulse (*ions-only* case) can be modeled by a differential equation of the form

$$\frac{d}{dt}N^{Cl_2{}^-}_I = \sum_{E,s}\left(-k_E - k^{DE}_s - k^{DI}_s - k^{DE}_g - k^{DI}_g\right)N^{Cl_2{}^-}_{E,s}, \tag{8}$$

where the decay rates $k^{DE/DI}_s$ and $k^{DE/DI}_g$ parametrically describe additionally possible losses of parent ions due to spontaneous decay from excited states s and due to residual gas collisions (g) leading to detachment (DE) or dissociation (DI), respectively.

The significance of an inhomogeneous loss mechanism can be illustrated for instance by assuming a simple analytical power dependence of the associated decay rate as $k_E \propto E^n$. In this case, it is easily shown that the number of parent ions decay as the power law depicted in Eq. (7), i.e., $N^{Cl_2{}^-}_I \propto t^{-1/n}$.

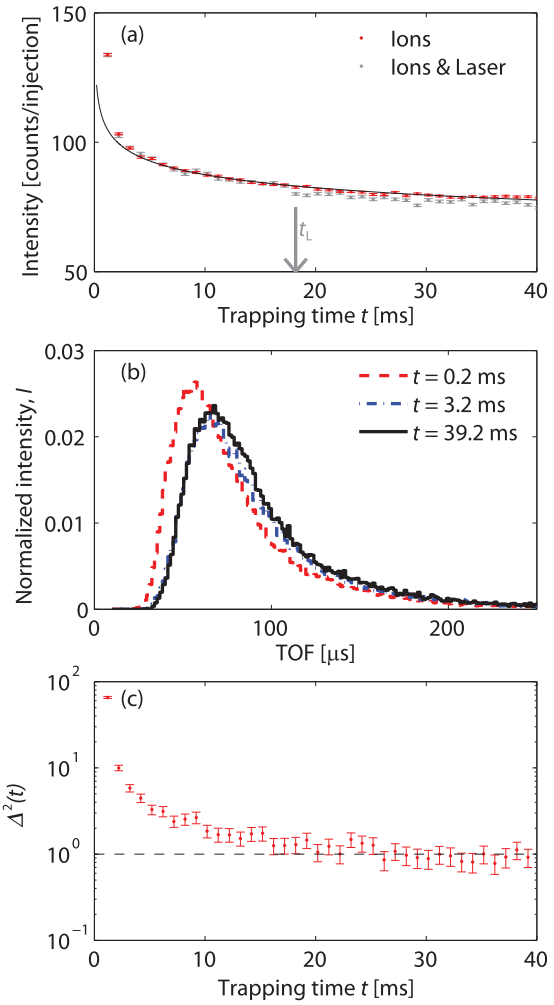

FIG. 5. (Color online) Trapping, laser-induced dissociation, and extraction of Cl_2^- (parent) with the combined RF trap and quadrupole mass spectrometer. (a) Total intensity of trapped Cl_2^- ions as a function of trapping time obtained by variation of the time of extraction of ions through the QMS. The red (dark) dots show the intensity obtained with only ions present in the RF trap, while the gray dots show the result when firing a laser pulse at $t_L = 18.2$ ms. (b) Time-of-flight distributions of Cl_2^- ions relative to the time of extraction from the RF trap. (c) Relaxation of the trapped ions as a function of trapping time illustrated by the convergence of the TOF distribution. The distributions are compared using the $\Delta^2(t)$ parameter defined in Eq. (9).

The evolution of the ensemble of trapped parent ions after injection was experimentally further explored by considering the time-of-flight distribution after extraction through the QMS. Examples of these distributions are shown in Fig. 5(b) for three different times of extraction. It is clearly seen that the TOF distributions evolve and peak at later times with increasing extraction time. Since more energetic (higher-E) ions travel faster through the QMS, this tendency can indeed be understood as evidence that the energy distribution of the trapped ions similarly evolves through primarily loss of the more energetic ions.

To quantify in more detail the evolution of the observed TOF distributions [Fig. 5(b)], we introduce the parameter

$$\Delta^2(t) = \frac{\sum_i [I(t,i) - I(t_r,i)]^2}{\sum_i \sigma^2(t,i) + \sigma^2(t_r,i)}, \tag{9}$$

where $I(t,i)$ and $I(t_r,i)$ are the number of counts in the ith time bin of the TOF distribution recorded at extraction time t and at a selected reference extraction time t_r, respectively. $\sigma(t,i)$ and $\sigma(t_r,i)$ are the statistical uncertainties for the ith time bin of these two TOF distributions, respectively. Clearly, the two distributions $I(t,i)$ and $I(t_r,i)$ become indistinguishable when $\Delta^2(t) \simeq 1$. Figure 5(c) displays the parameter $\Delta^2(t)$ evaluated for each point of the decay curve shown in Fig. 5(c), where $I(t_r,i)$ has been particularly selected to be the latest measured distribution at $t_r = 39.2$ ms. As seen, the value of $\Delta^2(t)$ decreases strongly until $t \sim 18$–20 ms after which time it is essentially constant with a value near unity. We interpret this finding as evidence that the translational properties of the sample of trapped ions evolve for ~20 ms after injection whereafter they can be considered stationary.

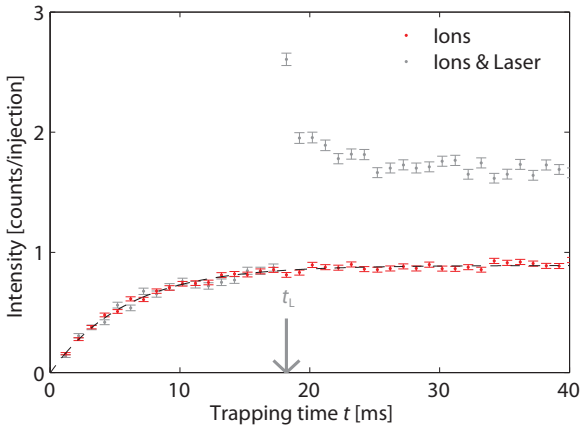

FIG. 6. (Color online) Trapping and laser-induced photodissociation of Cl_2^- ions to form Cl^- (daughter) ions. The intensity of daughter ions both without (red dots) and with (gray dots) the presence of a laser pulse at $t_L = 18.3$ ms is shown as a function of trapping time.

The red dots in Fig. 6 show the observed spontaneous evolution of the amount of *daugther* ions (Cl^-) observed as a function of trapping time. Using the model of Eq. (8), the evolution of the amount of trapped daughter ions can be explicitly written as

$$\frac{d}{dt} N_I^{Cl^-} = \sum_s \left(k_s^{DI} + k_g^{DI}\right) N_s^{Cl_2^-} - \sum_E k_E^d N_E^{Cl^-}, \tag{10}$$

where k_E^d now describes the loss rate of Cl^- due to their final energy after dissociation, and a model for the signal shown in Fig. 6 is hence obtained as

$$N_I^{Cl^-} = \int_0^t \frac{d}{dt} N_I^{Cl^-} dt, \tag{11}$$

where $t = 0$ is defined as the time when the trap is closed. As seen in Fig. 6, the intensity of trapped Cl^- ions increases during the first ca. 20 ms after which time it is essentially constant. The functional form of the measured curve is well represented by $N_I^{Cl^-} \propto (1 - e^{-t/\tau_{Cl^-}})$, with $\tau_{Cl^-} = 5.8 \pm 0.6$ ms.

The absolute amount of spontaneously produced daughter ions is significantly less than the amount of Cl_2^- ions lost from the trap as can be inferred by comparison to the Cl_2^- decay curve presented in Fig. 5(a). Hence, it seems likely that the loss of the parent beam by spontaneous dissociation (k_s^{DI}) or collisional-induced dissociation ($k_{\mathrm{g}}^{\mathrm{DI}}$) are only minor contributors to the total loss of Cl_2^- from the trap. It should be noted that the typical energy available in a binary collision of Cl_2^- and a rest gas molecule (say N_2) of mass m_{g}, i.e., $E_c = Em_{\mathrm{g}}/(m_{\mathrm{Cl}_2} + m_{\mathrm{g}}) \sim 0.3$ eV, which is significantly less than (however, of the same order of magnitude as) the dissociation energy of ground state Cl_2^- of $D_0 = 1.36$ eV [8]. We refrain from a further analysis of the origin of the spontaneous Cl^- in this paper, however, we wish to address similar spontaneous decays in a forthcoming paper. However, the fact that Cl^- is indeed produced spontaneously provides a very useful normalization of the laser-induced signal [see discussion leading to Eq. (18)].

B. Laser-induced dissociation

At a photon energy of 2.33 eV (532 nm), Cl_2^- ions in their electronic ground state can absorb directly to repulsive (dissociative) potential energy surfaces via the dipole-allowed $^2\Sigma_{\mathrm{u}}^+ \rightarrow {}^2\Pi_{\mathrm{g}}$ or $^2\Sigma_{\mathrm{u}}^+ \rightarrow {}^2\Sigma_{\mathrm{g}}^+$ transitions, while detachment to the ground state of Cl_2^0 ($^1\Sigma_{\mathrm{g}}^+$) is only energetically possible for very highly excited vibrational states of Cl_2^- ($^2\Sigma_{\mathrm{u}}^+$). Detailed potential energy curves for Cl_2^- can be found in Refs. [8,9].

The gray points in Fig. 5(a) show the evolution of trapped *parent* ions corresponding to the case of both ions and a laser pulse ($N_{\mathrm{IL}}^{\mathrm{Cl}_2^-}$) occurring at time $t_{\mathrm{L}} = 18.2$ ms during the trapping cycle. Evidently, when a laser pulse is present during the trapping cycle, a small but significant depletion of the parent ions is easily identified as the shift of the gray dots ($N_{\mathrm{IL}}^{\mathrm{Cl}_2^-}$) relative to the red dots ($N_{\mathrm{I}}^{\mathrm{Cl}_2^-}$) for $t \geqslant t_{\mathrm{L}}$. For the data shown in Fig. 5(a), the difference signal $\Delta N^{\mathrm{Cl}_2^-} = N_{\mathrm{IL}}^{\mathrm{Cl}_2^-} - N_{\mathrm{I}}^{\mathrm{Cl}_2^-}$ amounts to -2.2 ± 0.1 counts per injection when averaged over all times larger than t_{L}.

The pulse width of the laser ($w_{\mathrm{L}} \sim 3$ ns) is evidently much smaller than the time Δt needed for the spontaneous decay to cause a similar change of $N_{\mathrm{I}}^{\mathrm{Cl}_2^-}$, i.e., using Eq. (7)

$$\Delta t \approx \frac{\Delta N_{\mathrm{I}}^{\mathrm{Cl}_2^-}}{\frac{dN_{\mathrm{I}}^{\mathrm{Cl}_2^-}}{dt}} = \frac{\Delta N_{\mathrm{I}}^{\mathrm{Cl}_2^-}}{-A_0 \frac{1}{n}(t_{\mathrm{L}}/t_0)^{-1/n} t_{\mathrm{L}}^{-1}} = 5.6 \quad \mathrm{ms}. \tag{12}$$

Hence, the effect of the laser pulse can be well represented as an abrupt change of the number of stored ions, and modeled with the differential equation [expansion of Eq. (8)]

$$\frac{d}{dt} N_{\mathrm{IL}}^{\mathrm{Cl}_2^-} = \sum_{E,s} \left(-k_E - k_s^{\mathrm{DE}} - k_s^{\mathrm{DI}} - k_{\mathrm{g}}^{\mathrm{DE}} - k_{\mathrm{g}}^{\mathrm{DI}}\right) N_{E,s}^{\mathrm{Cl}_2^-} + \Delta N^{\mathrm{Cl}_2^-} \delta(t - t_{\mathrm{L}}), \tag{13}$$

where $\Delta N^{\mathrm{Cl}_2^-}$ is explicitly given by

$$\Delta N^{\mathrm{Cl}_2^-} = -\sigma_{\mathrm{L}} N_{\mathrm{I}}^{\mathrm{Cl}_2^-}(t_{\mathrm{L}}) \int n_{\mathrm{ph}}(x,y,z)\rho(x,y,z)dx\,dy\,dz. \tag{14}$$

Here, σ_{L} is the cross section for photodissociation, $n_{\mathrm{ph}}(x,y,z)$ is the photon number density, $\rho(x,y,z)$ is the normalized spatial density of trapped ions, and the integration extends over the total volume of the trap. It should be noted that Eq. (14) is stated under the assumption that the photodissociation cross section is the same for all trapped ions, but in general it depends on the initial state of the ion.

The gray dots in Fig. 6 display the corresponding time dependence of the number of Cl^- *daughter* ions when a laser pulse is present during storage. By analogy with Eq. (13), the evolution of the number of daughter ions can be written as [expanding Eq. (10)]

$$\frac{d}{dt} N_{\mathrm{IL}}^{\mathrm{Cl}^-} = \sum_s \left(k_s^{\mathrm{DI}} + k_{\mathrm{g}}^{\mathrm{DI}}\right) N_s^{\mathrm{Cl}_2^-} - \sum_E k_E^{\mathrm{d}} N_E^{\mathrm{Cl}^-} - \Delta N^{\mathrm{Cl}_2^-} \delta(t - t_{\mathrm{L}}), \tag{15}$$

while Eq. (11) still accounts for the observed integral signal. The enhanced daughter ion signal induced by the laser clearly decays within the first ~5 ms after exposure of the parent ions to laser light. This can be expected since the Cl^- fragments are released with a distribution of kinetic energies, and the most energetic fragment ions may then be able to escape the RF trap. Moreover, the trap depth for Cl^- is reduced as compared to Cl_2^- [Eq. (15) in [5]], and these two loss mechanisms are described by k_E^{d}, where E represents the total energy of the released fragment.

It should be noted that the absolute gain observed just after laser exposure corresponds quite well to the observed depletion of the parent ions. For the data shown in Fig. 6, the gain ΔN^{Cl^-} is 1.8 ± 0.1 while the corresponding depletion shown in Fig. 5(a) is $\Delta N^{\mathrm{Cl}_2^-} = -2.2 \pm 0.1 \approx -\Delta N^{\mathrm{Cl}^-}$.

C. Ion column density

To measure the column density of the trapped ions, a proper focusing of the laser beam is important. In the present setup, the laser beam is focused into the RF trap from a distance of ~1 m which is much larger than the longitudinal extent (along the z axis) of the trap (~50 mm). To a good approximation, the z dependence of the photon-number density can therefore be neglected across the trap, i.e., $n_{\mathrm{ph}}(x,y,z) = n_{\mathrm{ph}}(x,y)$. Moreover, the actual transverse width of the laser beam (diameter ~0.7 mm [see Fig. 4(c)] is relatively small compared to the length scale over which the ion density varies, and hence the ion density ρ can be assumed constant over the laser profile. With these assumptions, Eq. (14) can be simplified to

$$\begin{aligned}\Delta N^{\mathrm{Cl}_2^-} &= -\sigma_{\mathrm{L}} N_{\mathrm{I}}^{\mathrm{Cl}_2^-}(t_{\mathrm{L}}) \int \rho(x_L, y_L, z) \iint n_{\mathrm{ph}}(x,y)dx\,dy\,dz \\ &= -\sigma_{\mathrm{L}} N_{\mathrm{I}}^{\mathrm{Cl}_2^-}(t_{\mathrm{L}}) N_{\mathrm{ph}} \int \rho(x_L, y_L, z)dz,\end{aligned} \tag{16}$$

where $N_{\mathrm{ph}} = E_{\mathrm{p}}/E_\lambda$ is the number of photons. The integral in Eq. (16) represents the normalized column density $\rho_z(x_{\mathrm{L}}, y_{\mathrm{L}})$ of ions in the RF trap, which can hence be expressed directly as

$$\rho_z(x_{\mathrm{L}}, y_{\mathrm{L}}) = \frac{-\Delta N^{\mathrm{Cl}_2^-}}{\sigma_{\mathrm{L}} N_{\mathrm{I}}^{\mathrm{Cl}_2^-}(t_{\mathrm{L}}) N_{\mathrm{ph}}}. \tag{17}$$

Thus, assuming the same cross section for all ions, the column density of the trapped ions can be obtained from a measurement of the laser-induced depletion. Similarly, it can be obtained with a more favorable signal-to-background ratio from the enhanced daughter ion signal (see Fig. 6) since $\Delta N^{Cl^-} = -\Delta N^{Cl_2^-}$. In this case, however, the signal must be monitored promptly after laser exposure to avoid the aforementioned loss of fragment ions. Having demonstrated the feasibility of both these approaches [see Figs. 5(a) and 6], we decided in this work to investigate the column density of the trapped ions by measuring the laser-induced daughter ion signal just after exposure of the parent ions to laser light.

To obtain the ion column density, it is evident from Eq. (17) that the gain in daughter ion signal ΔN^{Cl^-} must be normalized to the number of parent ions present in the trap $N_I^{Cl_2^-}(t_L)$ at the time of laser exposure. This would entail switching the QMS between transmission of daughter ions and parent ions thereby making data acquisition more intricate and slow. However, as already mentioned, Cl^- is produced spontaneously which is reflected in $N_I^{Cl^-}$ being nonzero. The number of spontaneously produced fragment ions is directly proportional to number of injected Cl_2^- parent ions, that is $N_I^{Cl^-}(t_L) \propto N_I^{Cl_2^-}(t_L)$, and, consequently, if only the relative density is sought, there is no need to measure the number of parent ions. Thus, the final experimental quantity, proportional to the ion column density, is explicitly obtained as

$$\rho_z(x_L, y_L) \propto \frac{\Delta N^{Cl^-}(t_L)}{N_I^{Cl^-}(t_L) N_{ph}}, \tag{18}$$

which is measured as a function of the laser position (x_L, y_L). It must be noted that the quantities $N_I^{Cl^-}(t_L)$ and $N_{IL}^{Cl^-}(t_L)$ used in this expression to determine the laser-induced gain $\Delta N^{Cl^-}(t_L)$ and for parent normalization are naturally not obtained for the same trap loading, but for alternating loadings as described in the experimental section. However, the short-term variation in the number of trapped ions is indeed low and is suppressed when the data are averaged over several trap loadings.

Figures 7(a)–7(c) show two-dimensional plots of the column density obtained with a moderate step size of $\Delta x_L = \Delta y_L = 0.33$ mm, i.e., about equal to the spatial spread of the laser light in the trap region. The step size in these two-dimensional spectra are chosen relatively large in order to reveal major features while measuring at an affordable total number of different positions (here a grid of $25 \times 25 = 625$). Finer scans were done in single dimensions only. The column densities shown in Fig. 7 reveal clearly that the transverse distribution of ions in the RF trap is rather smooth and homogeneous, however, with an apparent (<10%) vertical asymmetry. Much stronger asymmetries have been observed in other multipole traps, i.e., a 22-pole trap [10], and have been explained [11] by minor mechanical misalignment of the RF poles.

The densities shown in Fig. 7 demonstrate moreover the effect of increasing the RF amplitude on the effective available trapping volume of the RF trap. At $V_0 = 300$ V [Figs. 7(a) and 7(d)] the trapped ion cloud seems to extend beyond the area accessible for the laser light, as defined by the rim of the end-cap electrode [black circles in Figs. 7(a)–7(c)], while at $V_0 = 700$ V [Figs. 7(c) and 7(f)] the ion cloud is fully confined

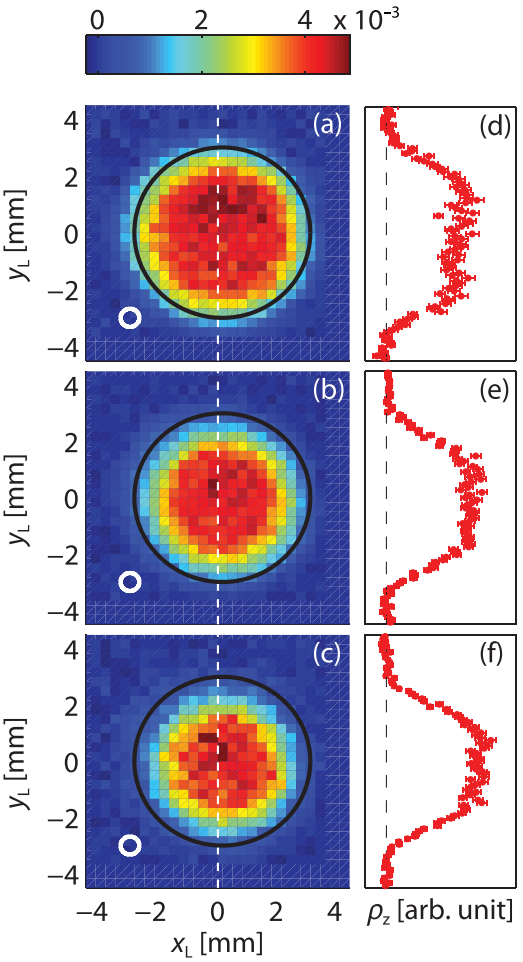

FIG. 7. (Color online) Ion densities for three different values of the RF amplitude, namely, (a), (d) $V_0 = 300$ V, (b), (e) $V_0 = 550$ V, and (b), (f) $V_0 = 700$ V. (a)–(c) Two-dimensional measurements of the ion column density. The black circles show the dimension of the end-cap electrode (6 mm diameter). The white ring shows the approximate extent of the laser profile (Fig. 4). (d)–(f) Fine scans of the column density in the vertical direction in steps much smaller than the width of the laser profile.

inside the region accessible by the laser. In all three cases, the ion column density is rather homogeneous and does not exhibit sharp structures.

A more quantitative view of the column densities recorded at the three different values of the RF amplitude is displayed in Figs. 7(d)–7(f). The one-dimensional scans of the densities along the central vertical axis were recorded with a step size of 0.092 mm which is much smaller than the width of the laser profile. These scans of finer resolution shown in Figs. 7(d)–7(f) in detail confirm the smoothness of the ion column density inferred from the two-dimensional scans.

IV. MODELING THE PARTICLE DISTRIBUTION

In the following, we seek to model the spatial distribution of ions in the trap by statistical mechanics methods. Initially, we establish a connection between the phase-space distribution and the energy distribution of an ensemble of particles moving in some general confining potential. To illustrate the

consequences of the derived relationship, a one-dimensional case study is presented, and finally the derived equations are employed to model the spatial ion distribution in the trap used in this experimental study.

A. Particle distribution in a Hamiltonian system

We consider a collection of a large number of identical and noninteracting particles moving in some general potential $U(\vec{r})$. In this case, the phase-space trajectory of a single particle is described by a Hamiltonian which has the same functional for all particles, namely,

$$H(\vec{r},\vec{p}) = \frac{p^2}{2m} + U(\vec{r}) = E, \tag{19}$$

where $\vec{p}$ and m are the momentum and mass, respectively, and E the mechanical energy of the particle. As the particles are noninteracting, the energy of a single particle is a conserved quantity, and the ensemble of particles is therefore a *microcanonical* ensemble since there is no energy exchange. The set of possible microstates for this ensemble can be represented by a set of points in phase space, and the probability distribution in phase space $f(\vec{r},\vec{p})$ then describes how the particles are distributed over the possible microstates. For an ensemble in equilibrium, f must be stationary. Liouville's theorem states that the phase-space distribution is stationary if the Poisson bracket of f and the Hamiltonian vanishes [12]. This is fulfilled if f is some function of the mechanical energy E. The probability to find a particle in a state with position and momentum coordinates in the intervals

$$\vec{r},\vec{r}+d\vec{r}, \quad \vec{p},\vec{p}+d\vec{p} \tag{20}$$

is therefore written as

$$f(\vec{r},\vec{p})\,d\vec{r}\,d\vec{p} = \frac{1}{Z}F(E(\vec{r},\vec{p}))d\vec{r}\,d\vec{p}. \tag{21}$$

Here, F is some function, and Z is the partition function found by normalizing the probability density, that is,

$$Z = \iint F(E(\vec{r},\vec{p}))d\vec{r}\,d\vec{p}. \tag{22}$$

To connect the phase-space weight function $F(E)$ to the energy distribution $P(E)$ of the ensemble, we first determine the phase-space volume Ω of a microstate with a certain energy ϵ. This quantity is expressed as

$$\begin{aligned}\Omega(\epsilon) &= \iint \delta[E(\vec{r},\vec{p}) - \epsilon]\,d\vec{r}\,d\vec{p} \\ &= 2\pi(2m)^{3/2}\int \sqrt{\epsilon - U(\vec{r})}\,d\vec{r},\end{aligned} \tag{23}$$

where Eq. (19) was used to change the integration from momentum to energy coordinates. Next, we transform the phase-space distribution from $(\vec{r},\vec{p})$ space to $(\vec{r},E)$ space. From Eq. (19), it is noted that f only depends on the magnitude of the momentum and not the individual momentum components, and therefore, we first transform the Cartesian momentum coordinates into spherical momentum coordinates which yields

$$f(\vec{r},p) = \frac{4\pi p^2}{Z}F(E(\vec{r},p)). \tag{24}$$

The momentum coordinate is then transformed into energy through Eq. (19), and by conservation of probability

$$\begin{aligned}f(\vec{r},E)d\vec{r}\,dE &= f(\vec{r},p(E))d\vec{r}\frac{dp}{dE}\,dE \\ &= \frac{2\pi(2m)^{3/2}}{Z}\sqrt{E-U(\vec{r})}\,F(E)\,d\vec{r}\,dE.\end{aligned} \tag{25}$$

The energy distribution is obtained by integration over the spatial coordinates

$$\begin{aligned}P(E) &= \int f(\vec{r},E)\,d\vec{r} \\ &= \frac{1}{Z}F(E)\,2\pi(2m)^{3/2}\int\sqrt{E-U(\vec{r})}\,d\vec{r} \\ &= \frac{\Omega(E)}{Z}F(E).\end{aligned} \tag{26}$$

If the energy distribution $P(E)$ is known, the corresponding weight function in phase space is consequently given as

$$F(E) = \frac{Z\,P(E)}{\Omega(E)} \tag{27}$$

leading to a phase-space density of

$$f(\vec{r},\vec{p}) = \frac{1}{Z}\frac{Z\,P(E(\vec{r},\vec{p}))}{\Omega(E(\vec{r},\vec{p}))} = \frac{P(E(\vec{r},\vec{p}))}{\Omega(E(\vec{r},\vec{p}))}. \tag{28}$$

If, instead, the ensemble is in contact and in thermal equilibrium with a heat bath of temperature T, the phase-space density is equal to the familiar *canonical* phase space density given by

$$f_c(\vec{r},\vec{p}) = \frac{\exp[-E(\vec{r},\vec{p})/kT]}{Z}. \tag{29}$$

It is therefore noted that the phase-space density of a canonical ensemble is identical to that of a microcanonical ensemble exhibiting an energy distribution of $P(E) \propto \Omega(E)\exp[-E/kT]$ despite the fact that the physical situations for the two ensembles are quite different.

Having established the phase-space density of an ensemble of a given energy distribution, the spatial distribution of the ensemble can now be determined by inserting Eq. (27) into (25) and integrating over all energies

$$\begin{aligned}\rho(\vec{r}) &= \int f(\vec{r},E)\,dE \\ &= 2\pi(2m)^{2/3}\int\sqrt{E-U(\vec{r})}\,\frac{P(E)}{\Omega(E)}\,dE.\end{aligned} \tag{30}$$

Finally, the column density is calculated by integrating out the z dependence of the spatial density

$$\rho_z(x,y) = \int \rho(\vec{r})dz. \tag{31}$$

B. One-dimensional case study

In order to make more clear the equations derived in the previous section and to highlight the major differences between a *canonical* ensemble and a *microcanonical* ensemble exhibiting a flat energy distribution, we here present phase-space and spatial distributions of such ensembles for a one-dimensional case study. It is assumed that particles of mass

$m = 70$ amu corresponding to Cl_2^- move in a one-dimensional potential $U_{\text{eff}}^{\text{1D}}(x)$ given by

$$U_{\text{eff}}^{\text{1D}}(x) \equiv U_{\text{eff}}(|x|/z_0, 0), \tag{32}$$

where U_{eff} is defined in Eq. (1). The fact that ion motion in this potential is only stable for $\eta \leqslant 0.3$ imposes the constraint that $x \leqslant x_{\max}$ where $x_{\max}$ is defined through the equation $\eta(x_{\max}/z_0, 0) = 0.3$. In turn, this requires that the mechanical energy E of a confined particle must be limited to

$$\frac{p^2}{2m} + U_{\text{eff}}^{\text{1D}}(x) = E(x,p) \leqslant U_{\text{trap}}^{\text{1D}} \equiv U_{\text{eff}}^{\text{1D}}(x_{\max}). \tag{33}$$

The effective potential and the quantities $x_{\max}$ and $U_{\text{trap}}^{\text{1D}}$ are displayed in Figs. 8(a) and 8(b).

The microcanonical ensemble is now considered to exhibit a flat energy distribution implying that

$$P_{\text{m}}(E) = \begin{cases} 0, & E > U_{\text{trap}}^{\text{1D}} \\ \frac{1}{U_{\text{trap}}^{\text{1D}}}, & E \leqslant U_{\text{trap}}^{\text{1D}}. \end{cases} \tag{34}$$

According to Eq. (28), the distribution in phase space for $E \leqslant U_{\text{trap}}^{\text{1D}}$ is written as

$$f_{\text{m}}(x,p) = \frac{P_{\text{m}}(E(x,p))}{\Omega_{\text{1D}}(E(x,p))} = \frac{1}{U_{\text{trap}}^{\text{1D}}\,\Omega_{\text{1D}}(E(x,p))}. \tag{35}$$

Here, Ω_{1D} is the one-dimensional equivalent of Eq. (23), that is,

$$\begin{aligned} \Omega_{\text{1D}}(\epsilon) &= \iint \delta[E(x,p) - \epsilon]\, dx\, dp \\ &= \sqrt{2m} \int_{-x_{\text{m}}(\epsilon)}^{x_{\text{m}}(\epsilon)} \frac{dx}{\sqrt{\epsilon - U_{\text{eff}}^{\text{1D}}(x)}}, \end{aligned} \tag{36}$$

where $x_{\text{m}}(\epsilon)$ is the maximum range of a particle with mechanical energy ϵ, that is, $\epsilon = U_{\text{eff}}^{\text{1D}}(x_{\text{m}}(\epsilon))$ [see Fig. 8(b)]. In Fig. 8(g), the phase-space volume given by Eq. (36) is plotted as a function of the mechanical energy when the RF amplitude is set to $V_0 = 750$ V, and the phase-space density for this microcanonical ensemble [Eq. (35)] is depicted in Fig. 8(d). As seen, the density is highest in the regions of high energy. This is due to the presence of the phase-space volume Ω_{1D} in the denominator of Eq. (35), a factor which decreases with energy.

For the canonical ensemble in contact with a heat bath of temperature T, the phase-space density for $E \leqslant U_{\text{trap}}^{\text{1D}}$ is given by

$$f_{\text{c}}(x,p) = \frac{\exp[-E(x,p)/kT]}{Z}, \tag{37}$$

where the partition function Z is expressed as

$$\begin{aligned} Z &= \iint \exp[-E/kT] dx\, dp \\ &= \int_0^{U_{\text{trap}}^{\text{1D}}} \Omega_{\text{1D}}(E) \exp[-E/kT] dE. \end{aligned} \tag{38}$$

The canonical phase-space distribution at a temperature of $T = 3000$ K is shown in Fig. 8(c). In contrast to the microcanonical density, the canonical density is high in phase-space regions where the energy is low.

The spatial distribution for the two ensembles is determined by integrating out the momentum dependence of the phase-space density, yielding

$$\begin{aligned} \rho(x) &= \int_{-p_{\max}(x)}^{p_{\max}(x)} f_\mu(x,p) dp \\ &= \sqrt{2m} \int_0^{U_{\text{trap}}^{\text{1D}}} \frac{f_\mu(x, p(E))}{\sqrt{[E - U_{\text{eff}}^{\text{1D}}(x)]}} dE, \end{aligned} \tag{39}$$

where $\mu = m$ *or* c and $p_{\max}(x) = \sqrt{2m[U_{\text{trap}}^{\text{1D}} - U_{\text{eff}}^{\text{1D}}(x)]}$ [see Figs. 8(a) and 8(c)]. The spatial distributions are shown in Figs. 8(e) and 8(f) for the canonical and the microcanonical ensembles, respectively. As seen, the spatial distributions are quite different: the canonical distribution peaks in the central region, whereas the microcanonical distribution is highest in the outer regions due to the larger contribution from energetic particles.

C. Ion distribution in the RF trap

In the following, the equations derived in Sec. IV A are applied to the case of an ensemble of ions trapped in a ring-electrode RF trap in order to model the spatial ion distribution. The adiabatic approximation for the motion of the trapped ions is assumed to be strictly valid, and if the effect of the static end-cap potential is neglected, the Hamiltonian describing the motion of a single ion is given by

$$H(x,y,z,\vec{p}) = \frac{p^2}{2m} + U_{\text{eff}}\left(\frac{r}{z_0}, \frac{z}{z_0}\right), \tag{40}$$

where $r = \sqrt{x^2 + y^2}$ and U_{eff} is the potential given by Eq. (1). When neglecting the end-cap potential, the trap is considered as being infinitely long, and since the electrode geometry is periodic in z with a period of $2\pi z_0$, z can be restricted to the interval $[0, 2\pi z_0]$. As already mentioned, the adiabatic approximation is only valid when the adiabaticity parameter η is below $\eta_{\max}$ which in turn gives rise to an effective trap depth U_{trap}. In this study, the trap depth is defined as the minimum of the effective potential in the nonadiabatic region, that is,

$$U_{\text{trap}}^{\text{eff}} = \min\{U_{\text{eff}}(\hat{r},\hat{z}) \,|\, \eta(\hat{r},\hat{z}) \geqslant \eta_{\max}\} \tag{41}$$

in accordance with model 1 of Ref. [5].

When the static end-cap potential is taken into consideration, the single-ion Hamiltonian is instead expressed as

$$\begin{aligned} H_{\text{tot}}(x,y,z,\vec{p}) &= \frac{p^2}{2m} + U_{\text{eff}}\left(\frac{r}{z_0}, \frac{z}{z_0}\right) + U_{\text{stat}}(r,z) \\ &= \frac{p^2}{2m} + U_{\text{tot}}(r,z), \end{aligned} \tag{42}$$

where U_{stat} is the static end-cap potential which is cylindrically symmetric and therefore only depends on r and z. In this case, not only the effective potential, but also the static potential contributes to the trap depth, and the total trap depth is therefore

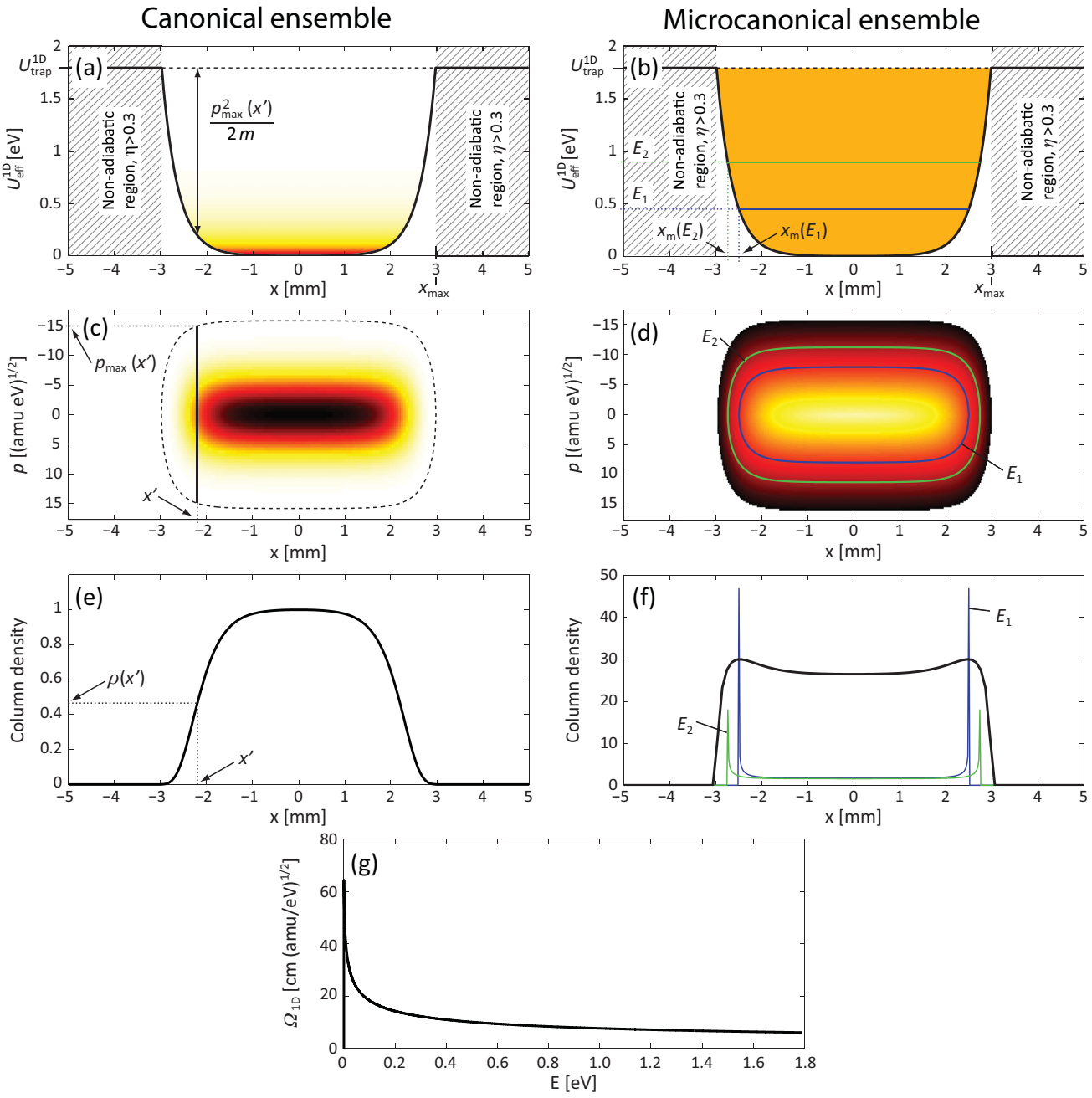

FIG. 8. (Color online) Characteristics of two ensembles: one (canonical) in contact with a heat bath of temperature $T = 3000$ K [(a), (c), (e)] and one (microcanonical) with a flat energy distribution [(b), (d), (f)]. (a), (b) The black curve displays the effective potential at $V_0 = 750$ V [Eq. (1)], and the hatched areas represent the regions where $\eta > 0.36$ [Eq. (2)] while color shadings represent the energy distribution of an ensemble (a) in contact with a heat bath $P(E) \propto \Omega(E)\exp(-E/kT)$, or (b) exhibiting a flat energy distribution $P(E)$ constant. In (b), two occupied energy levels E_1 (blue line) and E_2 (green line) are indicated. (c), (d) The color shading represents the phase-space density of an ensemble (c) in contact with a heat bath or (d) exhibiting a flat energy distribution. The dashed lines mark the trajectory of the phase space orbit with the highest allowed energy, that is, $E = U_{\text{trap}}^{\text{1D}}$. In (c), the black line indicates the momentum region to integrate over when the spatial density at x' is to be determined, and in (d) the blue and green lines show the phase-space trajectory of a particle with energy E_1 or E_2, respectively, corresponding to the energy levels shown in (b). (e), (f) The spatial distribution of an ensemble (e) in contact with a heat bath or (f) exhibiting a flat energy distribution. In (f), the blue and green lines display the spatial density of a particle with energy E_1 or E_2, respectively, corresponding to the energy levels shown in (b). (g) The phase-space volume Ω_{1D} [Eq. (36)] as a function of the mechanical energy.

expressed as

$$U_{\text{trap}}^{\text{tot}} = \min\left\{U_{\text{tot}}(r,z)\,\middle|\,\eta\left(\frac{r}{z_0},\frac{z}{z_0}\right) \geqslant \eta_{\max}\right\}. \qquad (43)$$

The first step in modeling the spatial ion distribution is to consider the distribution in phase space f in Eq. (21). In the present experimental study, the ions are isolated (not in contact with a buffer gas) and the ion ensemble can therefore

be considered as a microcanonical ensemble. Thus, the phase-space distribution is determined from the *mechanical* energy distribution of the ensemble as done in Eq. (28).

The actual mechanical energy within the adiabatic approximation is given by Eq. (42) when including the static end-cap potential. The mechanical energy distribution has not been determined experimentally, but simulations of the injection mechanism exploited here have provided information on the *kinetic* energy distribution [5]. These simulations which included the full time dependence of the trapping potentials revealed that when the ions first reach the trap center, their kinetic energy distribution at high RF amplitudes is approximately uniform with some low-energy cutoff, E_0.[1] To calculate the spatial distribution according to Eq. (30), the simulated *kinetic* energy distribution of the time-dependent problem must be related to the *mechanical* energy distribution within the adiabatic approximation. In the expression [Eq. (42)] for the mechanical energy, the first term represents the kinetic energy stored in the smooth drift motion while the second term U_{eff} actually represents the kinetic energy stored in the micromotion (see [2]). Thus, the first two terms in Eq. (42) merely represent the *total* kinetic energy of the stored ion within the time-dependent picture. As the static potential is negligible at the trap center, the aforementioned uniform *kinetic* energy distribution does in fact reflect the *mechanical* energy distribution of the trapped ions, which is therefore assumed to be

$$P(E) = \begin{cases} \frac{1}{U^{\mu}_{\text{trap}} - E_0}, & E_0 \leqslant E \leqslant U^{\mu}_{\text{trap}} \\ 0, & \text{otherwise.} \end{cases} \tag{44}$$

Here, E_0 is the low-energy cutoff of the uniform distribution, and $\mu =$ tot or eff depending on whether or not the static end-cap potential is taken into consideration. The spatial density is then calculated according to Eq. (30), yielding

$$\rho(\vec{r}) = 2\pi(2m)^{2/3} \int_{E_0}^{U^{\mu}_{\text{trap}}} \frac{\sqrt{E - U_{\mu}(\vec{r})}}{\left[U^{\mu}_{\text{trap}} - E_0\right]\Omega(E)} dE. \tag{45}$$

Here, the density of states $\Omega(E)$ is calculated from Eq. (23) where U is substituted by U_{μ}. Finally, the ion column density is determined by integrating out the z dependence of the spatial distribution according to Eq. (31).

Figures 9(a) and 9(b) display the spatial three-dimensional ion density in the (y,z) plane and the ion column density of Cl_2^- ions trapped at a RF amplitude of $V_0 = 550$ V. In both cases, $\eta_{\max} = 0.36$ while $E_0 = 20$ meV and the potentials of the left and right end caps were set to -27 and -228 V, respectively. As seen, the maximum of the density in the (y,z) plane is pushed towards the left as the potential applied to the left end cap is less repulsive than that applied to the right end cap. Furthermore, the periodic ring-electrode array is imaged into the spatial density that shows a spatial distance between successive local maxima or minima equal to the minimum spatial separation of neighboring electrodes irrespective of their RF phase. Since microstates of almost any energy up to the trap depth are populated, the spatial density is seen to extend all the way out to the nonadiabatic region, the boundary of which is indicated by white solid lines. The column density shown in Fig. 9(b) is very smooth, rather flat in the central regions, and extends all the way out to the nonadiabatic region. For comparison, the thermal spatial and column densities are shown in Figs. 9(c) and 9(d) at the same trapping parameters as those used in Figs. 9(a) and 9(b) and at a temperature of $T = 300$ K. In this case, the ions are more confined in space, as the more energetic microstates are suppressed due to $U^{\text{tot}}_{\text{trap}} = 1.8$ eV being much larger than $kT = 26$ meV.

Figure 10 shows in detail the model column density profiles along the x or y axis for three RF amplitudes. As seen, the ion cloud compresses as the RF amplitude is increased due to the fact that the region of adiabatic motion shrinks with increasing amplitudes. For all three amplitudes, the ion density is almost constant in a large central region.

To verify that the above model provides a good description of the ion spatial density, we also performed numerical simulations of ion trajectories during trapping. For a given trajectory to come close to every point in its accessible phase space, the trajectory must be propagated for a sufficiently long-time interval in accordance with the ergodic hypothesis. As traditional integration methods such as the fourth-order Runge-Kutta methods accumulate error in energy which can be quite severe when integrating over long times [13] we developed a code for propagating the trajectories using an eighth-order symplectic integrator suitable for long-time integration [14]. This integrator is suited for Hamiltonian systems and therefore the Hamiltonian of Eq. (42) was employed to describe ion motion inside the trap, implying that the effect of the RF trapping field was described in terms of the time-independent analytical effective potential of Eq. (1). The end-cap electrode potential was derived by use of the SIMION 8.0 software [15]. The trajectories of numerous ions with randomized initial conditions were integrated for a time span of 240 μs, and during the integration of each orbit, the ion position and energy were stored at random times. The Monte Carlo ensemble resulting from this procedure does not represent the actual stored ion ensemble as the energy distributions of the two ensembles are not the same. Sets of position and energy coordinates from the Monte Carlo ensemble were then removed randomly to create an ensemble with an energy distribution matching that of Eq. (44). The resulting column densities from these simulations are shown in Fig. 10 together with the column densities obtained from statistical mechanical principles. As seen, the two model densities agree to a high degree, thereby validating our statistical approach to describing the ion spatial distribution in the adiabatic approximation.

V. DISCUSSION

1. *Properties of the trapped ions*

To gain insight on the properties of ions trapped in the RF trap when using the newly described mechanism of injection [5], the experimental evidence collected in the recorded time evolution of the parent ions (Fig. 5) and the detailed scans of

[1]The low-energy cutoff arises since an ion must be traveling on the trap central axis and entering the trap at a very specific point in time in order to arrive at the trap center with exactly zero energy. Consequently, the probability for trapping ions with very low energy is small.

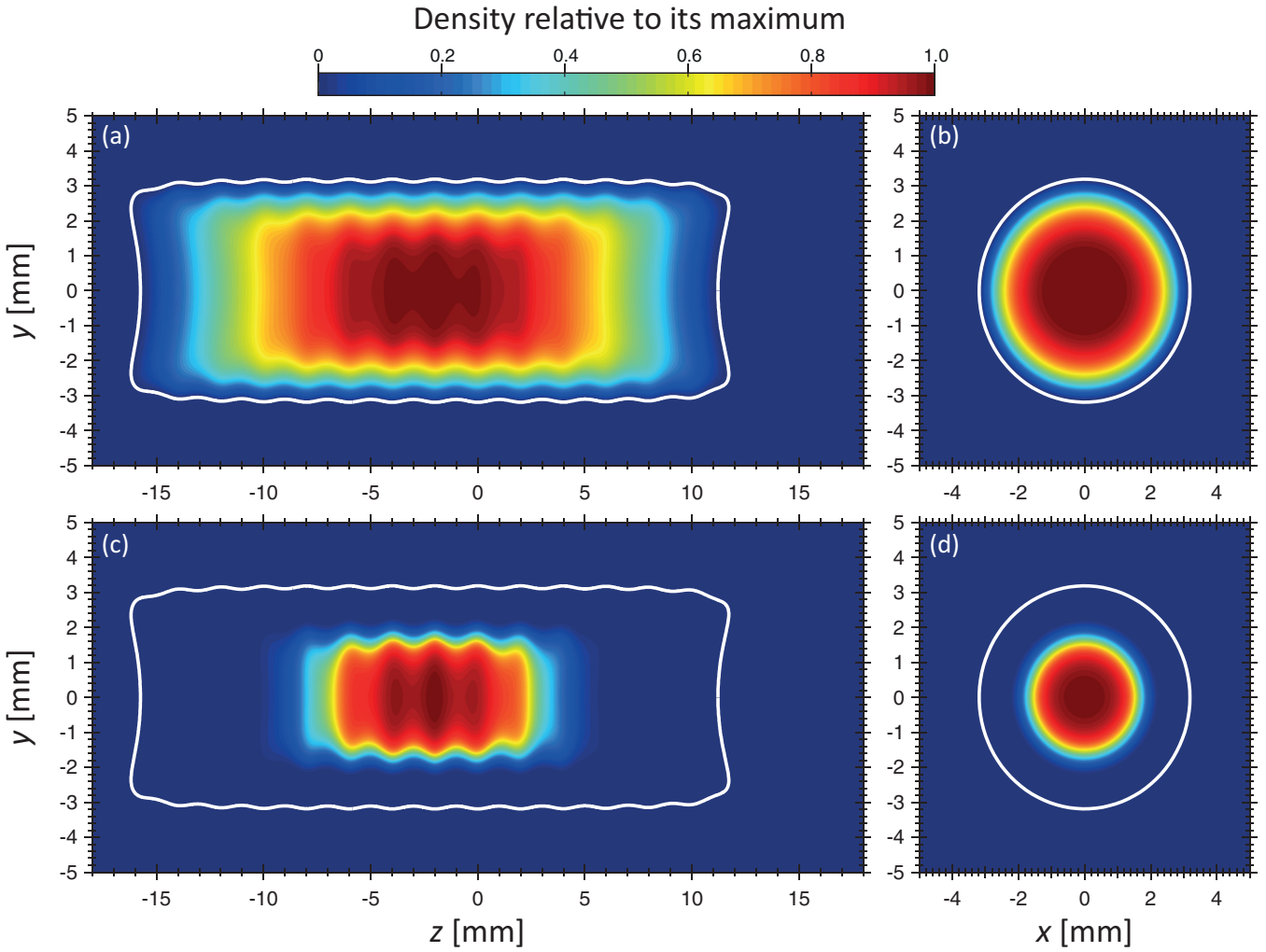

FIG. 9. (Color online) Spatial ion densities of Cl_2^- ions trapped at a RF amplitude of $V_0 = 550$ V and $\eta_{max} = 0.36$. The static potentials applied to the left and right end caps are -27 and -228 V, respectively. The low-energy cutoff is set to $E_0 = 20$ meV. All densities are depicted relative to their respective maximum. (a) Ion density in the (y,z) [or (x,z)] plane for a *microcanonical* ensemble with the energy distribution given by Eq. (44) and (b) the column density as a function of x and y for the same ensemble. (c) Ion density in the (y,z) [or (x,z)] plane for a *canonical* ensemble of temperature $T = 300$ K and (d) the column density as a function of x and y for the same ensemble. In all graphs, the white line shows the boundary between the adiabatic and nonadiabatic regions.

the column density [Eq. (18)] shown in Figs. 7(d)–7(f) can be discussed under different assumptions of ion dynamics in the RF trap after the short ($\sim$100 μs) period of injection.

The newly described mechanism of injection of ions into the ring-electrode RF trap [5] is mediated by the acceleration or deceleration of the approaching ions by the longitudinal component (along the trap central axis) of the electric field generated by the oscillating RF trapping potentials. The consequence is that the energy distribution of the trapped ions is a function of both the RF amplitude V_0 and the offset (nominal energy) $K_{stat} = K_0 - q\,V_{trap}$ ($\sim$3 eV for the setting applied here) of the RF-trap platform potential V_{trap} relative to initial kinetic energy K_0 of the approaching ions. The expected resulting *initial* ion energy distributions [5] for the setting applied in this work is broad ($\sim$0–5 eV) and essentially uniform [5].

It should be emphasized that contrary to previously described multipole RF traps where buffer gas (typically He) at a certain temperature T is used to decelerate and thermalize ions inside the trap, i.e., the phase-space distribution follows a Boltzmann distribution [see Eq. (29)], the expected distribution of energies in the present situation is obviously *not* expected to be thermal. However, the well-established results for thermalized ensembles of ions in multipole RF traps provide an interesting comparison to the results observed here.

2. *Loss of parent ions*

In 22-pole traps using He buffer gas for thermalization, the number of trapped parent ions has been found to decay *exponentially* with time [16] and the decay mechanism has been described as evaporation of ions from the trap [16]. In detail, at low RF amplitudes (<20 V in Refs. [16,17]) ion evaporation occurs because the ions in the high-energy tail of the Boltzmann distribution are too energetic to be confined by the effective potential ($\eta < 0.36$ [16]) and hence escape the

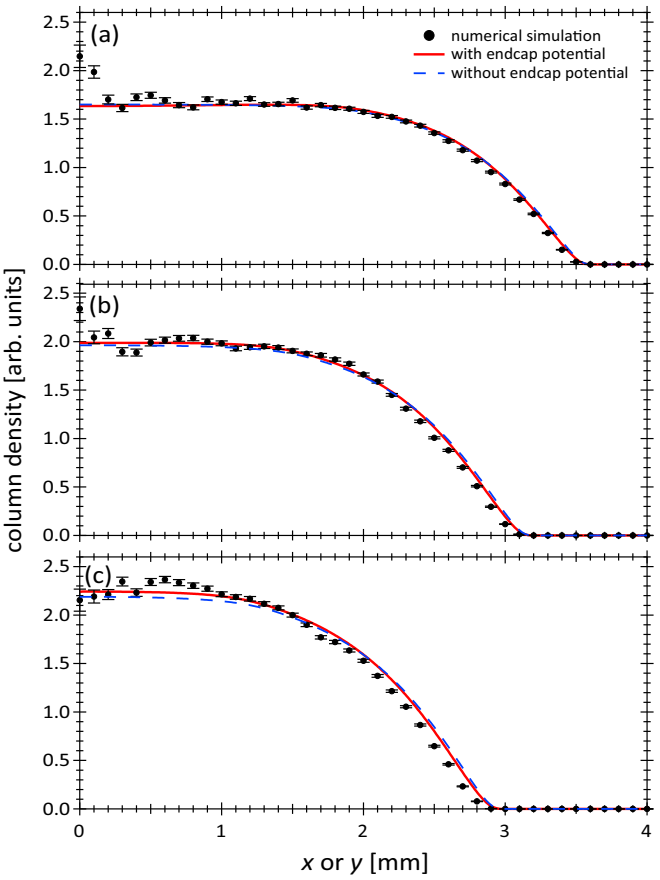

FIG. 10. (Color online) Ion column densities at three different RF amplitudes: (a) $V_0 = 300$ V, (b) $V_0 = 550$ V, and (c) $V_0 = 750$ V. The dashed blue lines and solid red lines represent the column density modeled by statistical mechanics excluding and including the static end-cap potential, respectively. The black circles represent the column density according to numerical simulations of ion motion in the time-independent potential U_{tot}. In all cases, $\eta_{\max}$ was set to 0.36.

trap. At higher RF amplitudes, spatial regions in which the adiabatic approximation breaks down start to emerge and ions entering these regions are able to exchange energy with the RF field which leads to ion loss [16,17].

The exponential decay observed for this *thermalized* ensemble implies that the ion decay is homogeneous in the sense that all ions on average have the same decay rate. This situation arises as the individual properties of the ions are constantly changed (reset) by collisions with the buffer gas, and this constant randomization of the ion energy happens at a rate of 10^5 s^{-1} [16] in the aforementioned experiments.

The case described with the present setup is entirely different since the trapped ions have essentially negligible collision rates and momentum exchange with the residual gas as well as among themselves (ion density $\sim$40cm^{-3}), and thus the trapped ions interact mainly with the applied electric fields. Therefore, in terms of the loss of parent ions, the individual properties [in particular, the mechanical energy E given by Eq. (42)] of the trapped ion are expected to determine its decay rate, and consistently a decay following a power law [Eq. (7)] is observed for the parent ions.

The energy-dependent mechanism of ion loss seems likely to originate from energy exchange with the oscillating RF field: hence, the more energetic ions come closer to the boundaries of the trap where the adiabatic approximation breaks down, and in these regions the ions may experience energy gain leading to escape from the trap or energy loss leading to stabilization in the trap. When injecting ions into the trap with a broad energy distribution as done here, it is consequently expected that the high-energy part of the distribution is depleted faster, thereby cooling the ensemble. As seen in Fig. 5(b), the peak of the TOF distribution of the extracted ions moves towards later arrival times during trapping, and Fig. 5(c) shows that the TOF distribution mainly evolves during the first $\sim$20 ms for Cl_2^- of trapping. These findings are indeed consistent with depletion of the high-energy part of the energy distribution.

3. *Spatial distribution of trapped ions*

When considering the spatial distribution of a thermalized ensemble of ions in RF traps, the significance of the mutual ion-ion Coulomb repulsion (space charge) is often quantified through the value of the the so-called coupling parameter $\Gamma = q^2/(4\pi E_0 a k_{\mathrm{B}} T)$, where the distance a is defined from the ion density as $a = (3n/4\pi)^{1/3}$ [18]. The coupling parameter thus measures the ratio of the average Coulomb repulsion to average kinetic energy, and for $\Gamma \ll 1$ evidently the effects of space charge can be ignored. Since the present experiments do not concern thermalized ensembles of ions, a strict evaluation of Γ is not meaningful, however, with ion densities of typically $n \sim 40$ cm^{-3} and mechanical energies of the trapped ion range up to a few eV, space-charge effects can safely neglected for the present experiments.

The particle distribution in RF traps has been described and investigated for *thermalized* ensembles of ions both for cases with small coupling parameter (i.e., low ion densities or high temperature) [11] and for higher coupling parameter (high densities or low temperature) [18,19]. In particular for multipole traps, spatial profiles (tomography) were first measured in an octupole trap [20,21] using a laser-induced flourescence signal from trapped Ba^+ ions. Later measurements have exploited depletion of negative ions by photodetachment [11,22] and laser-induced dissociation [19,23], similar to this study.

In the low-density limit, relevant for the comparison to the present results, recent experiments performed with a 22-pole trap [11] have shown that strong spikelike variations of the longitudinal ion column density can occur due to imperfections in the mechanical construction. As seen in Fig. 7, the distributions observed with the present ring-electrode trap are essentially homogeneous with only a small vertical asymmetry. This asymmetry may indeed also result from a minor misalignment of the two opposing electrodes that forms the ring structure seen by the ions (see Fig. 11 of Ref. [5] for a detailed illustration).

The measured column densities are now compared to the model column density derived from Eq. (45) which assumes that the ion density is low such that ion-ion interactions can be neglected. To obtain a model for the measured density $\rho_{\mathrm{z,m}}$ at the position $(0, y_{\mathrm{L}})$, the model density ρ_{z} must be folded

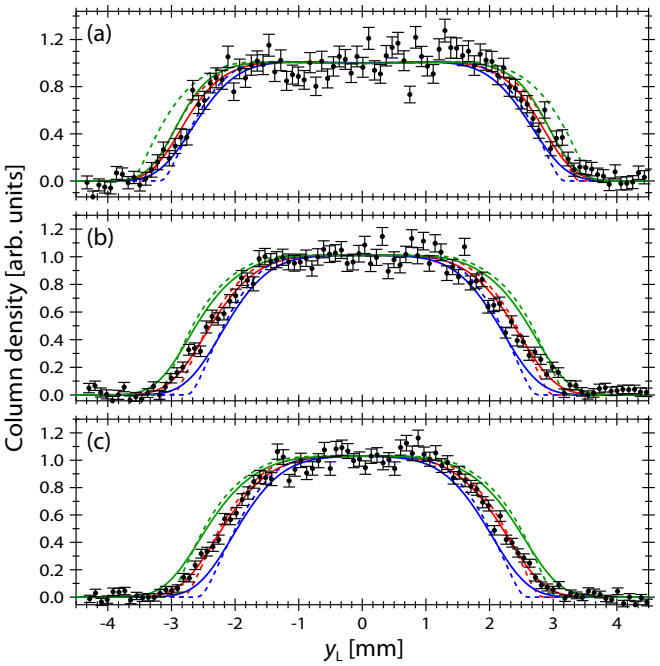

FIG. 11. (Color online) Ion column densities at three different RF amplitudes: (a) $V_0 = 300$ V, (b) $V_0 = 550$ V, and (c) $V_0 = 700$ V. The black circles represent the experimentally determined column densities (see also Fig. 7), the dashed lines the column density modeled by statistical mechanics, and the solid lines the modeled column density folded by the laser profile and the geometrical constraint imposed by the end-cap electrode [see Eq. (46)]. The red curves represent the calculated profiles that provide the best simultaneous fit to the three measured profiles yielding $\eta_{max} = 0.284 \pm 0.009$ and $E_0 = 27 \pm 10$ meV. The blue curves represent the calculated profiles for $\eta_{max} = 0.2$ and $E_0 = 27$ meV, while the green curves represent the calculated profiles for $\eta_{max} = 0.4$ and $E_0 = 27$ meV.

with the laser profile, and also the geometrical constraint imposed by end-cap electrode must be taken into account. Thus, the model density relevant for comparison with the data is calculated according to

$$\rho_{z,m}(0, y_L) \propto \int g_y(y - y_L)\rho_z(0, y)H(y_{cap} - |y|)\,dy, \qquad (46)$$

where H is the Heaviside step function. Figure 11 shows the three experimental profiles from Figs. 7(d)–7(f) overlayed with the calculated column densities for three different values of η_{max} and for a low-energy cutoff of $E_0 = 27$ meV. The calculated profiles were fitted to the experimental ones by varying η_{max} and E_0 which were restricted to the same values for all three profiles. The best fit yields $\eta_{max} = 0.284 \pm 0.009$ and $E_0 = 27 \pm 10$ meV, and calculated profiles at these values are represented by the solid red lines in the figure. As seen, the experimental and calculated profiles agree to a very high extent, and the small uncertainty in η_{max} obtained from the fit is reflected in the fact that the model profiles for $\eta_{max} = 0.2$ (blue curve) and $\eta_{max} = 0.4$ (green curve) provide poor descriptions of the measured profiles for the two largest RF amplitudes.

As mentioned in Sec. IV C, the low-energy cutoff E_0 is introduced since an ion must enter the trap at a very specific point in time in order to arrive at the trap center with exactly

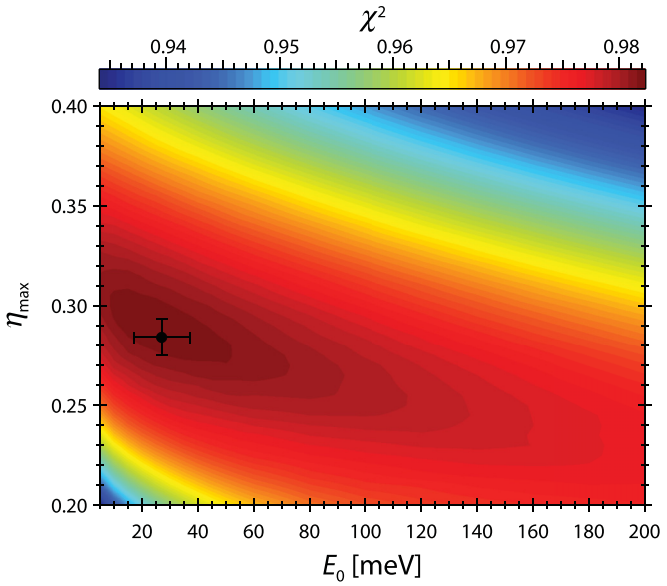

FIG. 12. (Color online) The goodness-of-fit parameter χ^2 as a function of the maximum value of the adiabaticity parameter η_{max} and the low-energy cutoff of the energy distribution E_0. The black point indicates with uncertainties the values of E_0 and η_{max} obtained from the best fit of the model to the experimental data.

zero energy. Therefore, the probability for trapping ions with extremely low energy is small. Although in principle ions could still be trapped initially with zero kinetic energy, minor jitter in the trap supplies and the Coulomb repulsion between the ions would prevent ions from staying trapped with zero kinetic energy. Hence, the existence of E_0 is justified, but its value is more evasive. To examine the correlation between the low-energy cutoff E_0 and η_{max}, a contour plot of the goodness-of-fit parameter χ^2 as a function of E_0 and η_{max} is presented in Fig. 12. As seen, η_{max} decreases with increasing E_0 which can readily be explained: as E_0 increases, the low-energy states are slowly removed thereby shifting the density towards the outer regions. Consequently, η_{max} (which controls the spatial extent of the ion cloud through the trap depth) must be lowered in order to keep the same apparent width of the profile. As already stated, the best fit to the data yields $E_0 = 27 \pm 10$ meV and $\eta_{max} = 0.284 \pm 0.009$ which is indicated by the black point in Fig. 12. Overall, the obtained value of η_{max} is in good agreement with the generally accepted value of 0.3.

In the first investigations of ion trapping using the injection mechanism described in Ref. [5], the maximum adiabaticity parameter was estimated from the measured trapping efficiency to be $\eta_{max} = 0.64$. This value is in significant excess of the values of $\eta_{max} = 0.3$ [2] or 0.36 [16] previously reported to characterize the stable region of multipole RF traps. Furthermore, from the model densities presented in Fig. 11, it is clear that the experimental column densities can not in fact reflect a maximum adiabaticity parameter of $\eta_{max} = 0.64$. Thus, the experimental results indicate a significant energy exchange between the ions and the oscillating electric fields for an extended period of time after closing the trap. This energy exchange provides an overall energy relaxation which finally

leads to trapping in the region governed by a smaller value of the maximum adiabaticity parameter around 0.28. However, the total trapping efficiency reported earlier seems to indicate that ions initially are trapped with energies corresponding to $\eta_{\max} = 0.64$.

As already stated, the energy distribution of the trapped ions $P(E)$ used in the model density is not explicitly measured in this work, but inferred from simulations. However, it would be very interesting in a future experiment to probe this distribution since it would allow us to deduce more precisely a value for $\eta_{\max}$ for the present trap. It might seem straightforward already at this point to probe the energy distribution by using the quadrupole mass filter as a retarding energy analyzer as done in similar experimental setups (see, for example, Ref. [24]). In the present setup, the longitudinal RF field at the trap entrance modulates the energy distribution of the ions as they enter the trap and, similarly, the longitudinal RF field at the trap exit might affect the energy distribution of the extracted ions. It is therefore not obvious that the energy distribution measured by using the quadrupole mass filter would be representative of the ion energy distribution in the trap. Another approach could be to probe the ion energy distribution *inside* the trap by Doppler spectroscopy of, e.g., trapped Ca^+ or Mg^+ ions, where the photoabsorption intensity could be monitored by fluorescence detection, which we indeed wish to implement in future studies.

A. Time-resolved mass spectrometry

In Figs. 5(a) and 6 we showed the experimentally determined temporal evolution of the number of parent and daughter ions during trapping and after the presence of a laser pulse at a selected time. Viewed together, the depletion signal observed for parent ions (Cl_2^-) [Fig. 5(a)] and the corresponding gain in the dissociation products (Fig. 6) illustrate an important methodological possibility of the present setup, namely, the ability to perform *time-resolved mass spectrometry* where both the loss of the parent ions as well as the gain of daughter ions can be monitored.

For the present simple Cl_2^- system, the total laser-induced loss of parent ions and the corresponding gain of daughter ions agrees when measured immediately after exposure to light (see Sec. III B). For laser-induced processes that are prompt relative to the round-trip time in the RF trap (typically 20 μs), this correspondence allows us to deduce not only the total absorption cross section for the parent ions (see Sec. V B), but also reliable fraction branching ratios into channels producing various daughter ions. This is of relevance to many molecular ions as generally several dissociation pathways will be open after photoabsorption.

In future studies, we will explore this possibility of time-resolved mass spectrometry in particular for molecular ions irradiated by synchrotron radiation from the ASTRID2 facility [25]. Under irradiation with energetic ionizing synchrotron radiation, we expect the present method (see Fig. 2) to become advantageous since injection of parent ions can be done efficiently without the use of buffer gas. A possible relative dense buffer gas would strongly ionize under extreme ultraviolet (XUV) irradiation providing a high density of reactive ions in the trap which moreover would alter the trapping conditions (space charge) and finally could cause detection problems.

A clear advantage of the present method of time-resolved mass spectrometry is that the extraction time t_E can be set freely relative to the laser pulse time (t_L) allowing us to follow the evolution of the fragment channels on the microsecond time scale. This is in contrast to, for instance, another recently developed method of time-resolved mass spectrometry based on fast ion beams in a storage ring, where the time resolution is defined by the ion revolution time in the instrument [26]. Furthermore, high (variable) mass resolution is obtained due to the extraction of the ions through the QMS, the resolution of which can be adapted to the studied system. For the present study of Cl_2^-, only a poor resolution was applied (see Fig. 3), giving on the other hand high transmission and thereby shorter measuring times. Moreover, the current method of time-resolved mass spectrometry is very sensitive since only a very few counts per injection ($\ll 1$) provide sufficient measurable signal. Especially, very weak fragmentation channels will be identifiable since the background of daughter ions is generally small. Here, the spontaneously decaying Cl_2^- ions from the ANIS source are probably to be regarded as an exception or a peculiarity of the production in the sputtering process [27]. Finally, the decay of the daughter ion signal after photodissociation shown in Fig. 6 in fact contains information on the kinetic energy of the trapped ions.

Of course, a general setback of the method is the inability to detect directly produced neutral fragments and photoelectrons. However, another potential use of the present setup is to prepare specific daughter ions based on photofragmentation of a trapped precursor parent ion. After irradiation of the parent ions, the produced daughter ions could be extracted through the QMS and reaccelerated to form a fast beam for further experiments. The feasibility of this approach naturally relies on the ability of generating a sufficient number of product ions for the envisioned experiment.

B. Absolute cross section

In addition to the potential of the present method to characterize photon-induced molecular reactions in terms of relative absorption intensity and fragment branching ratios, scanning of the laser light across the transverse plane of the trap also allows for determination of absolute cross sections. This is directly seen from Eq. (17) for the column density at laser position (x_L, y_L). Hence, integration of Eq. (17) over the laser position leads to a closed expression for the cross section as

$$\sigma_L = \frac{1}{N_{ph}} \int \frac{-\Delta N^{Cl_2^-}}{N_I^{Cl_2^-}(t_L)} dx_L dy_L, \tag{47}$$

where the right-hand side contains measurable quantities only. All the quantities in this expression can not be determined in a single trap loading, as the laser-induced depletion $\Delta N^{Cl_2^-}$ is obtained essentially as the difference between the number of trapped Cl_2^- ions with and without the presence of laser light. However, as already mentioned, short-term variations in the number of trapped ions are negligible and do not limit the determination of the absolute cross section.

This method is similar to the depletion tomography method [10,22,28] developed previously to measure absolute cross sections for photodetachment of anions in a 22-pole trap. In these studies, the induced change of the observed *exponential* decay rate constant of trapped parent ions when applying laser pulses during trapping was measured across the transverse plane of the trap. The present method [Eq. (47)] differs on one central aspect compared to these studies, namely, that it only requires to measure the relative change $[\Delta N_{\mathrm{I}}^{\mathrm{Cl_2}^-}/N_{\mathrm{I}}^{\mathrm{Cl_2}^-}(t_{\mathrm{L}})]$ of parent (daughter) ion induced by the laser. For each laser position, this ratio only needs to be measured shortly after the exposure of the parent ions to the laser light, whereas the aforementioned method relies on measuring an assumed exponential decay law of the trapped parent ions for each laser position. Thus, apart from making no assumptions on the decay law of trapped parent ions, the method presented here should also be faster in terms of measurement time.

Furthermore, the column densities obtained in this study are smooth compared to recent studies in a 22-pole trap [10] where strong variations across the trap were observed due to slight imperfections in the mechanical construction [11]. The fact that the variation of the column density is rather smooth and homogeneous (see Fig. 7) in the present trap makes scanning with a moderate step size feasible compared to a profile dominated by sharp structure, where evidently the step size must be adapted to be much smaller than the extent of the structures. In the present setup, the ion cloud is not sensitive to minor modifications of the trapping potential since the ion ensemble contains ions of energies comparable to the trap depth. However, if the translational degrees of freedom are cooled to 10 K as in the aforementioned case of the 22-pole trap, it can not be excluded that structures in the column density appear as a result of, for example, minor mechanical misalignments. Finally, it should be noted that the determination of absolute cross section using the formalism in Eq. (47) is most accurate when applied to the depletion signal [Fig. 5(a)].

Although it is possible to extract an absolute cross section from the data shown in Figs. 7(c) and 7(f), we refrain here from stating an actual number since the initial state distribution of the ion ensemble delivered from the ion source is unknown and no effort was made here to manipulate or characterize it.

VI. CONCLUSION

With this study, we have further explored the experimental possibilities arising from the trapping of ions in a RF trap without the use of a dense buffer gas for initial ion deceleration. While advantageous in many respects, the use of dense buffer gas becomes problematic in combination with ionizing agents such as XUV radiation from the upcoming ASTRID2 synchrotron radiation facility [25] for which the present experimental setup is intended to be used.

We have demonstrated that upon injection with the newly described mechanism [5], a dilute ion cloud of Cl_2^- trapped in the RF field relaxes (cools) within ∼20 ms and afterwards occupies a volume of the trap consistent with the range predicted by a maximum adiabaticity parameter of $\eta_{\mathrm{max}} \sim 0.28$.

Furthermore, we have shown that the experimental setup is suited for time-resolved mass spectrometry on fragmenting molecular ions, and indicated the possibly of absolute-cross-section measurements with a tomographic method without the restrictive assumption on the decay law for the trapped parent ions.

ACKNOWLEDGMENTS

H.B.P. acknowledges support from the Lundbeck foundation. A.S. acknowledges for support from the Carlberg foundation. Discussions with Professor J. Ulrik Andersen are greatly appreciated.

[1] W. Paul, O. Osberghaus, and E. Fischer, Forschungsber. Wirtsch.-Verkehrminist Nordrhein-Westfalen **415**, 1 (1958).
[2] D. Gerlich, in *State-Selected and State-to-State Ion-Molecule Reaction Dynamics. Part 1: Experiment*, Advances in Chemical Physics Series, Vol. LXXXII, edited by C.-Y. Ng and M. Baer (Wiley, New York, 1992), pp. 1–176.
[3] R. Wester, J. Phys. B: At., Mol. Opt. Phys. **42**, 154001 (2009).
[4] O. Asvany and S. Schlemmer, Int. J. Mass Spectrom. **279**, 147 (2009).
[5] A. Svendsen, L. Lammich, J. E. Andersen, H. K. Bechtold, E. Søndergaard, F. Mikkelsen, and H. B. Pedersen, Phys. Rev. A **87**, 043410 (2013).
[6] M. Weiss, in *Proceedings of CAS School: Fifth General Accelerator Physics Course*, Vol. 94-01, edited by S. Turner (CERN, Meyrin, Switzerland, 1994), pp. 913–953.
[7] H. Andersen and P. Tykesson, IEEE Trans. Nucl. Sci. **22**, 1632 (1975).
[8] J. G. Dojahn, E. C. M. Chen, and W. E. Wentworth, J. Phys. Chem. **100**, 9649 (1996).
[9] E. C. M. Chen and W. E. Wentworth, J. Phys. Chem. **89**, 4099 (1985).
[10] P. Hlavenka, R. Otto, S. Trippel, J. Mikosch, M. Weidemüller, and R. Wester, J. Chem. Phys. **130**, 061105 (2009).
[11] R. Otto, P. Hlavenka, S. Trippel, J. Mikosch, K. Singer, M. Weidemüller, and R. Wester, J. Phys. B: At., Mol. Opt. Phys. **42**, 154007 (2009).
[12] F. Schwabl, *Statistical Mechanics* (Springer, Berlin, 2006).
[13] H. Yoshida, IAU Symposia **152**, 407 (1992).
[14] H. Yoshida, Phys. Lett. A **150**, 262 (1990).
[15] SIMION 8.0, Scientific Instrument Services, Inc., Ringoes, NJ.
[16] J. Mikosch, U. Frühling, S. Trippel, R. Otto, P. Hlavenka, D. Schwalm, M. Weidemüller, and R. Wester, Phys. Rev. A **78**, 023402 (2008).
[17] J. Mikosch, U. Frühling, S. Trippel, D. Schwalm, M. Weidemüller, and R. Wester, Phys. Rev. Lett. **98**, 223001 (2007).
[18] C. Champenois, J. Phys. B: At., Mol. Opt. Phys. **42**, 154002 (2009).

[19] T. Majima, G. Santambrogio, C. Bartels, A. Terasaki, T. Kondow, J. Meinen, and T. Leisner, Phys. Rev. A **85**, 053414 (2012).
[20] R. D. Knight and M. P. Prior, J. Appl. Phys. **50**, 3044 (1979).
[21] H. Schaaf, U. Schmeling, and G. Werth, Appl. Phys. **25**, 249 (1981).
[22] S. Trippel, J. Mikosch, R. Berhane, R. Otto, M. Weidemüller, and R. Wester, Phys. Rev. Lett. **97**, 193003 (2006).
[23] P. H. Hemberger, N. S. Nogar, J. D. Williams, R. G. Cooks, and J. E. P. Syka, Chem. Phys. Lett. **191**, 405 (1992).
[24] K. M. Ervin and P. B. Armentrout, J. Chem. Phys. **83**, 166 (1985).
[25] N. Hertel and S. V. Hoffmann, Synch. Radiat. News **24**, 19 (2011).
[26] K. Støchkel, U. Kadhane, J. U. Andersen, A. I. S. Holm, P. Hvelplund, M.-B. S. Kirketerp, M. Koefoed-Larsen, M. K. Lykkegaard, S. B. Nielsen, S. Panja, and H. Zettergren, Rev. Sci. Instrum. **79**, 023107 (2008).
[27] J. Fedor, K. Hansen, J. U. Andersen, and P. Hvelplund, Phys. Rev. Lett. **94**, 113201 (2005).
[28] T. Best, R. Otto, S. Trippel, P. Hlavenka, A. von Zastrow, S. Eisenbach, S. Jezouin, R. Wester, E. Vigren, M. Hamberg, and W. D. Geppert, Astrophys. J. **742**, 63 (2011).